

agreement with the recent results from the Wilkinson Microwave Anisotropy Probe (WMAP) which indicate that the first onset of star formation most probably occurred at redshifts $z \approx 15\text{--}20$ (~ 250 Myr after the Big Bang)^{25–27}.

The presence of Ly α emitting galaxies and luminous quasars at the end of cosmic reionization ($z > 6.0$), at a time when the IGM was at least 1% neutral, was clearly demonstrated^{5,28}. This epoch of reionization represents a key benchmark in cosmic structure formation, indicating the formation of the first luminous structures. Detecting a large reservoir of molecular gas in this epoch demonstrates the existence of the requisite fuel for active star formation in primeval galaxies. The existence of such reservoirs of molecular gas at early times implies that studies of the youngest galaxies will be possible at millimetre and centimetre wavelengths, unhindered by obscuration by the neutral IGM. □

Received 16 May; accepted 16 June 2003; doi:10.1038/nature01821.

- Ohta, K. *et al.* Detection of molecular gas in the quasar BR1202-0725 at redshift $z = 4.69$. *Nature* **382**, 426–428 (1996).
- Omont, A. *et al.* Molecular gas and dust around a radio-quiet quasar at redshift 4.69. *Nature* **382**, 428–431 (1996).
- Carilli, C. L. *et al.* High-resolution imaging of molecular line emission from high redshift QSOs. *Astron. J.* **123**, 1838–1846 (2002).
- Carilli, C. L. & Blain, A. W. Centimeter searches for molecular line emission from high-redshift galaxies. *Astrophys. J.* **569**, 605–610 (2002).
- Fan, X. *et al.* A survey of $z > 5.7$ quasars in the Sloan Digital Sky Survey. II. Discovery of three additional quasars at $z > 6$. *Astron. J.* **125**, 1649–1659 (2003).
- White, R. L., Becker, R. H., Fan, X. & Strauss, M. A. Probing the ionization state of the universe at $z > 6$. *Astron. J.* (in the press).
- Willott, C. J., McLure, R. L. & Jarvis, M. J. A $3 \times 10^9 M_{\odot}$ black hole in the quasar SDSS J1148 + 5251 at $z = 6.41$. *Astrophys. J.* **587**, L15–L18 (2003).
- Loeb, A. & Barkana, R. The reionization of the Universe by the first stars and quasars. *Annu. Rev. Astron. Astrophys.* **39**, 19–66 (2000).
- Bertoldi, F. *et al.* Dust emission from the most distant quasars. *Astron. Astrophys. Lett.* (in the press).
- Bertoldi, F. *et al.* Molecular gas in the host galaxy of a quasar at redshift $z = 6.42$. *Astron. Astrophys.* (in the press).
- Solomon, P. M., Radford, S. J. E. & Downes, D. Molecular gas content of the primeval galaxy IRAS 10214 + 4724. *Nature* **356**, 318–321 (1992).
- Strong, A. W. *et al.* Diffuse continuum gamma rays from the Galaxy observed by COMPTEL. *Astron. Astrophys.* **292**, 82–91 (1994).
- Downes, D. & Solomon, P. Rotating nuclear rings and extreme starbursts in ultra-luminous galaxies. *Astrophys. J.* **507**, 615–654 (1998).
- Weiss, A., Neinger, N., Huttemeister, S. & Klein, U. The effect of violent star formation on the state of the molecular gas in M82. *Astron. Astrophys.* **365**, 571–587 (2001).
- Solomon, P. M., Downes, D., Radford, S. J. E. & Barrett, J. W. The molecular inter-stellar medium in ultraluminous infrared galaxies. *Astrophys. J.* **478**, 144 (1997).
- Ferrarese, L. & Merritt, D. A fundamental relation between supermassive black holes and their host galaxies. *Astrophys. J.* **539**, L9–L12 (2000).
- Gebhardt, K. *et al.* A relationship between the nuclear black hole mass and galaxy velocity dispersion. *Astrophys. J.* **539**, L13–L16 (2000).
- Richards, G. T. *et al.* Broad emission-line shifts in quasars: an orientation measure for radio-quiet quasars? *Astron. J.* **124**, 1–17 (2002).
- Haiman, Z. & Cen, R. A constraint on the gravitational lensing magnification and the age of the redshift $z = 6.28$ quasar SDSS 1030 + 0524. *Astrophys. J.* **578**, 702–707 (2001).
- Elvis, M. *et al.* Atlas of quasar energy distributions. *Astrophys. J. (Suppl.)* **95**, 1–68 (1995).
- Telfer, R. C., Zheng, W., Kriss, G. A. & Davidsen, A. F. The rest-frame extreme-ultraviolet spectral properties of quasi-stellar objects. *Astrophys. J.* **565**, 773–785 (2002).
- Pentericci, L. *et al.* VLT optical and near-infrared observations of the $z = 6.28$ quasar SDSS J1030 + 0524. *Astron. J.* **123**, 2151–2158 (2002).
- Heger, A. & Woosley, S. E. The nucleosynthetic signature of population III. *Astrophys. J.* **567**, 532–543 (2002).
- Arnett, A. Massive star evolution and SN 1987A. *Astrophys. J.* **383**, 295–307 (1991).
- Cen, R. Implications of WMAP observations on the population III star formation processes. *Astrophys. J. Lett.* (submitted).
- Kogut, A. *et al.* Wilkinson Microwave Anisotropy Probe (WMAP) first year observations: TE polarization. *Astrophys. J.* (submitted).
- Spergel, D. N. *et al.* First year Wilkinson Microwave Anisotropy Probe (WMAP) observations: determination of cosmological parameters. *Astrophys. J.* (submitted).
- Hu, E. M. *et al.* A redshift $z = 6.56$ galaxy behind the cluster Abell 370. *Astrophys. J.* **568**, L75–L79 (2002).

Acknowledgements The VLA is operated by the National Radio Astronomy Observatory (NRAO), a facility of the National Science Foundation (NSF), operated under co-operative agreement by Associated Universities, Inc. (AUI). This work is based partly on observations carried out with the IRAM Plateau de Bure Interferometer. IRAM is supported by INSU/CNRS (France), MPG (Germany) and IGN (Spain). F.W. is a Jansky Fellow.

Competing interests statement The authors declare that they have no competing financial interests.

Correspondence and requests for materials should be addressed to F.W. (fwalter@nrao.edu).

Rotational actuators based on carbon nanotubes

A. M. Fennimore*, T. D. Yuzvinsky*, Wei-Qiang Han*, M. S. Fuhrer*†, J. Cumings*† & A. Zettl*

* Department of Physics, University of California at Berkeley, and Materials Sciences Division, Lawrence Berkeley National Laboratory, Berkeley, California 94720, USA

Nanostructures are of great interest not only for their basic scientific richness, but also because they have the potential to revolutionize critical technologies. The miniaturization of electronic devices over the past century has profoundly affected human communication, computation, manufacturing and transportation systems. True molecular-scale electronic devices are now emerging that set the stage for future integrated nanoelectronics¹. Recently, there have been dramatic parallel advances in the miniaturization of mechanical and electromechanical devices². Commercial microelectromechanical systems now reach the submillimetre to micrometre size scale, and there is intense interest in the creation of next-generation synthetic nanometre-scale electromechanical systems^{3,4}. We report on the construction and successful operation of a fully synthetic nano-scale electromechanical actuator incorporating a rotatable metal plate, with a multi-walled carbon nanotube serving as the key motion-enabling element.

The overall size scale of our actuator is of the order of ~ 300 nm and its components are integrated on a silicon chip. Low-level externally applied voltages precisely control the operation speed and position of the rotor plate. Repeated oscillations of the rotor plate between positions 180° apart, as well as rotations of 360° , have been demonstrated with no signs of wear or fatigue. Unlike existing chemically driven bio-actuators and bio-motors, our fully synthetic nanometre-scale electromechanical system (NEMS) actuator is designed to operate over a wide range of frequency, temperature, and environmental conditions, including high vacuum and harsh chemical environments.

Although devices have been made by scaling down existing microelectromechanical systems (MEMS), the workhorse methods and materials of MEMS technology are not universally well suited to the nanoscale. Ultra-small silicon-based systems fail to achieve desired high-Q mechanical resonances owing to dominant surface effects and thermoelastic damping, and limitations in strength and flexibility compromise silicon-based high-performance actuators^{5,6}. On the other hand, the unusual mechanical and electronic properties of carbon⁷ and boron-nitride⁸ nanotubes (including favourable elastic modulus and tensile strength, high thermal and electrical conductivity, and low inter-shell friction of the atomically smooth surfaces^{9,10}) suggest that nanotubes may serve as important NEMS-enabling materials.

Figure 1a shows the conceptual design of the electromechanical rotational actuator. The rotational element (R), a solid rectangular metal plate serving as a rotor plate, is attached transversely to a suspended support shaft. The support shaft ends are embedded in electrically conducting anchors (A1, A2) that rest on the oxidized surface of a silicon chip. The rotor plate assembly is surrounded by three fixed stator electrodes: two 'in-plane' stators (S1, S2) are horizontally opposed and rest on the silicon oxide surface, and the third 'gate' stator (S3) is buried beneath the surface. Four independent (d.c. and/or appropriately phased a.c.) voltage signals, one to the rotor plate and three to the stators, can be applied to

† Present addresses: Department of Physics, University of Maryland, College Park, Maryland 20742-4111, USA (M.S.F.); Department of Physics, Stanford University, Stanford, California 94305-4045, USA (J.C.).

control the position, speed and direction of rotation of the rotor plate. The key component in the assembly is a single multi-walled carbon nanotube (MWNT), which serves simultaneously as the rotor plate support shaft and the electrical feedthrough to the rotor plate; most importantly it is also the source of rotational freedom.

Our NEMS actuator was constructed using lithographic methods. MWNTs, synthesized by the standard arc technique¹¹, were suspended in 1,2-dichlorobenzene and deposited on degenerately doped silicon substrates covered with 1 μm of SiO_2 . The nanotubes were located with respect to pre-patterned alignment marks on the SiO_2 surface using an atomic force microscope or a LEO 1550 scanning electron microscope (SEM). The remaining actuator components (in-plane rotor plate, in-plane stators, anchors, and electrical leads) were then patterned using electron beam lithography. A single layer of electron beam resist (polymethyl methacrylate, 950,000 relative molecular mass, 5.5% in chlorobenzene) was spun on the samples at 4,000 r.p.m. for 45 seconds, and subsequently baked in air at 150 $^\circ\text{C}$ for 2 hours. The resist was then patterned using NPGS software on a JEOL 6400 SEM, and developed in methyl isobutyl ketone:isopropyl alcohol 1:3 for one minute. Gold (~ 90 nm) with a chromium adhesion layer (~ 10 nm) was then thermally evaporated and lifted off in acetone. The Cr/Au was subsequently annealed at 400 $^\circ\text{C}$ to ensure better electrical and mechanical contact between the Cr and the MWNT. An HF etch was used to remove roughly 500 nm of the SiO_2 surface to provide clearance for the rotor plate once it was rotated by 90 $^\circ$. The conducting Si substrate (typically used as the gate electrode in three-terminal nanotube field-effect devices^{12,13}) here serves as the

gate stator. Figure 1b shows an actuator device prior to etching. Typical rotor plate dimensions were 250–500 nm on a side.

Initial actuator characterization was carried out *in situ* inside the SEM. We found that applying voltages up to 50 V d.c. between the (slightly asymmetric) rotor plate and the gate stator generated a net torque sufficient to visibly rotate the rotor plate (up to 20 $^\circ$ deflection). When the applied voltage was removed, the rotor plate would rapidly return to its original horizontal position. Using a finite analysis program (FEMLAB, a commercially available plug-in for MATLAB) and our actuator geometry together with the measured deflection and applied voltages, we determine for our devices typical ‘as produced’ effective torsional spring constants of 10^{-15} to 10^{-12} N m. Evaluation of the MWNT shear modulus (assuming a continuum mechanics model¹⁴) necessitates knowledge of the outer radii of the nanotubes. We were able to determine the outer diameter of the MWNTs in our devices to within 20%, and found that they ranged from 10 to 40 nm, which was consistent with high-resolution transmission electron microscopy (TEM) measurements of MWNTs from the same preparation batch. TEM imaging also showed the MWNTs to be of high structural quality, composed of concentrically nested cylindrical tubules with no obvious defects. For a 10-nm-diameter MWNT with an effective length of 2 μm , we estimate a shear modulus of 100 to 300 GPa. These ranges for torsional spring constant and shear modulus overlap those of more direct measurements employing a suspended MWNT subjected to torsional deflection via an atomic force microscope tip^{15,16}.

Although the actuator devices just described have a number of extremely useful characteristics (including predicted torsional oscillator mechanical resonance frequencies of the order of tens to hundreds of megahertz), the strong torsional spring constant effectively prevents large low-frequency angular displacements. For large-displacement operation, we modified the MWNT support shaft in an attempt to exploit the intrinsic low-friction bearing behaviour afforded by the perfectly nested shells of MWNTs^{9,10,17,18}. The modification consists of removing or compromising one or more outer MWNT shells in the region between the rotor plate and the anchors. Several *in situ* methods were used to achieve the modification in the SEM, including reactive-ion etching, application of current through the nanotube to ‘blow out’ outer nanotube shells^{19,20}, and selective nanotube bond-damage

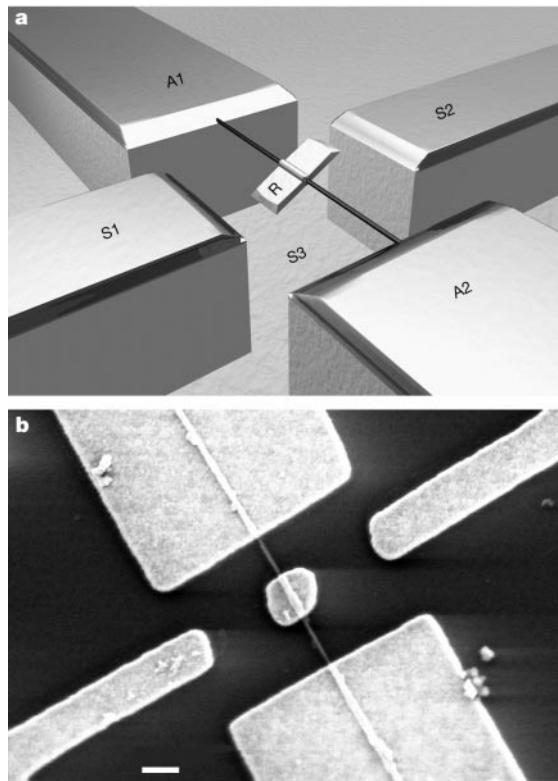


Figure 1 Integrated synthetic NEMS actuator. **a**, Conceptual drawing of nanoactuator. A metal plate rotor (R) is attached to a multi-walled carbon nanotube (MWNT) which acts as a support shaft and is the source of rotational freedom. Electrical contact to the rotor plate is made via the MWNT and its anchor pads (A1, A2). Three stator electrodes, two on the SiO_2 surface (S1, S2) and one buried beneath the surface (S3), provide additional voltage control elements. The SiO_2 surface has been etched down to provide full rotational freedom for the rotor plate. The entire actuator assembly is integrated on a Si chip. **b**, Scanning electron microscope (SEM) image of nanoactuator just prior to HF etching. The actuator components can be identified by comparing this image to **a**. Scale bar, 300 nm.

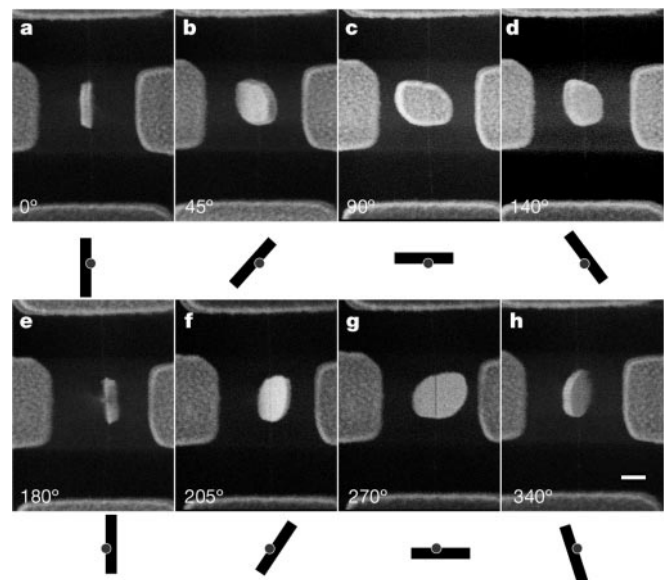


Figure 2 Series of SEM images showing the actuator rotor plate at different angular displacements. The MWNT, barely visible, runs vertically through the middle of each frame. The schematic diagrams located beneath each SEM image illustrate a cross-sectional view of the position of the nanotube/rotor-plate assembly. Scale bar, 300 nm.

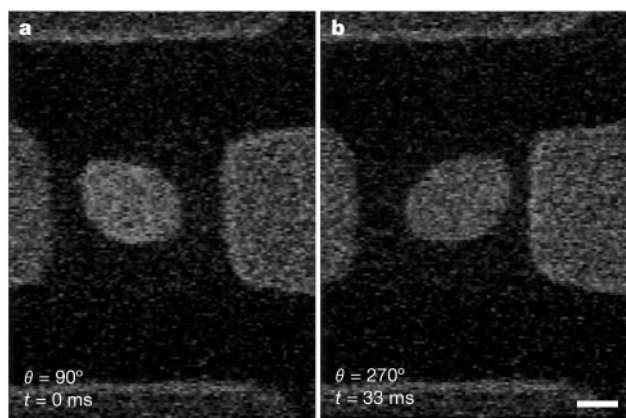


Figure 3 Two SEM images captured from a video recording of an a.c.-voltage-driven actuator ‘flipping’ between the extremal horizontal positions (90° and 270°). The two images are taken one video frame (that is, 33 ms) apart. (See Supplementary Information.) Rapid, large-amplitude rotor plate oscillations could be sustained nearly indefinitely with no noticeable wear or degradation in actuator operation. The MWNT is not visible in these images, but it runs vertically through the middle of each frame. Scale bar, 300 nm.

induced by the SEM electron beam.

A particularly simple yet effective *in situ* MWNT modification method, and the one used on the devices to be described below, was to mechanically fatigue and eventually shear the outer nanotube shells by successive application of very large stator voltages. We found that applied gate stator voltages of order 80 V d.c. would torque the outer nanotube shells past the elastic limit, eventually leading to partial or complete failure of the outer nanotube shells and a resulting dramatic increase in the rotational freedom of the rotor plate. In the ‘free’ state, the rotor plate was still held in position axially by the intact nanotube core shells, but could be azimuthally positioned, using an appropriate combination of stator signals, to any arbitrary angle between 0° and 360°. Once so positioned, the rotor plate nominally remained in place even with all stator voltages reduced to zero, eventually drifting to a vertical (0° or 180°) position only under the charging influence of the SEM imaging electron beam.

Figure 2 shows a series of still SEM images recorded of an actuator device in the free state, being ‘walked’ through one complete rotor plate revolution using quasi-static d.c. stator voltages. The stator voltages, never exceeding 5 V, were adjusted sequentially to attract the rotor plate edge to successive stators. By reversing the stator voltage sequence, the rotor plate rotation could be reproducibly reversed.

Finite frequency operation of the actuator was also performed, using a variety of suitably phased a.c. and d.c. voltage signals to the three stators and rotor plate. In one simple operation mode, we applied out-of-phase common-frequency sinusoidal voltages to stators S1 and S2, a doubled-frequency signal to S3, and a d.c. offset to the rotor plate R; that is, $S1 = V_0 \sin(\omega t)$, $S2 = V_0 \sin(\omega t - \pi)$, $S3 = V_0 \sin(2\omega t + \pi/2)$, $R = -V_0$. Although the resulting spatial and temporal drive forces are actually quite complex, roughly speaking this sequence allowed the rotor plate to be sequentially electrostatically attracted to the next available stator. Using this drive sequence we were reliably able to alternately flip the rotor plate between the extreme horizontal (90° and 270°) positions. Although in principle very high frequency operation should be possible (restricted only by the stripline bandwidth of the leads and, ultimately, inertial effects of the rotor plate), our SEM image capture rate limited direct real-time observations of rotor plate oscillations to frequencies of typically several hertz.

We found that the transitions between the extreme horizontal positions could be made faster than the image video capture rate of 33 ms. Figure 3 shows two images of the actuator, recorded 33 ms apart, showing the rotor plate respectively in the 90° and 270°

positions. We were able to rotationally drive actuators in this fashion for many thousands of cycles, with no apparent wear or degradation in performance. (See Supplementary Information.) In this configuration, the MWNT clearly serves as a reliable, presumably wear-free, NEMS element providing rotational freedom. This characterization was performed in a pressure of 10^{-6} – 10^{-5} torr, although we anticipate reliable operation at higher pressures. We note that our actuator is the first true MWNT-based NEMS device, in that it fully integrates electronic control and mechanical response. This distinguishes it from previous related MWNT-based mechanical devices which require relatively large and complex external control systems (such as piezo-driven manipulators) to achieve operation^{15–18,21}.

Our MWNT-based actuators have obvious MEMS/NEMS applications potential. The rotational metal plate could serve as a mirror, with obvious relevance to ultra-high-density optical sweeping and switching devices (our total actuator size is just at the limit of visible light focusing). The rotating plate could also serve as a paddle for inducing and/or detecting fluid motion in microfluidics systems, as a gated catalyst in wet chemistry reactions, as a bio-mechanical element in biological systems, or as a general (potentially chemically functionalized) sensor element. It is also possible that the charged oscillating metallic plate could be used as a transmitter of electromagnetic radiation. Using methods to align nanotubes, it should be possible to fabricate arrays of orientationally ordered nanotube-based actuators on substrates. □

Received 4 April; accepted 10 June 2003; doi:10.1038/nature01823.

1. Tour, J. M. *et al.* Recent advances in molecular scale electronics. *Ann. NY Acad. Sci.* **852**, 197–204 (1998).
2. Judy, J. W. Microelectromechanical system (MEMS): Fabrication, design and applications. *Smart Mater. Struct.* **10**, 1115–1134 (2001).
3. Craighead, H. G. Nanoelectromechanical systems. *Science* **290**, 1532–1535 (2000).
4. Roukes, M. L. in *Tech. Digest of the 2000 Solid-State Sensor and Actuator Workshop* (eds Bousse, L. & Schmidt, M.) 367–376 (Transducer Research Foundation, Cleveland, 2000).
5. Carr, D. W., Evoy, S., Sekaric, L., Craighead, H. G. & Parpia, J. M. Measurement of mechanical resonance and losses in nanometer scale silicon wires. *Appl. Phys. Lett.* **75**, 920–922 (1999).
6. Lifshitz, R. & Roukes, M. L. Thermoelastic damping in micro- and nanomechanical systems. *Phys. Rev. B* **61**, 5600–5609 (2000).
7. Iijima, S. Helical microtubules of graphitic carbon. *Nature* **354**, 56–58 (1991).
8. Chopra, N. G. *et al.* Boron nitride nanotubes. *Science* **269**, 966–967 (1995).
9. Charlier, J.-C. & Michenaud, J.-P. Energetics of multilayered carbon tubules. *Phys. Rev. Lett.* **70**, 1858–1861 (1993).
10. Kolmogorov, A. N. & Crespi, V. H. Smoothest bearings: Interlayer sliding in multiwalled carbon nanotubes. *Phys. Rev. Lett.* **85**, 4727–4730 (2000).
11. Ebbesen, T. W. & Ajayan, P. M. Large-scale synthesis of carbon nanotubes. *Nature* **358**, 220–222 (1992).
12. Tans, S. J. *et al.* Individual single-wall carbon nanotubes as quantum wires. *Nature* **386**, 474–477 (1997).
13. Bockrath, M. *et al.* Single electron transport in ropes of carbon nanotubes. *Science* **275**, 1922–1925 (1997).
14. Yakobson, B. I., Brabec, C. J. & Bernholc, J. Nanomechanics of carbon tubes: Instabilities beyond linear response. *Phys. Rev. Lett.* **76**, 2511–2514 (1996).
15. Williams, P. A. *et al.* Torsional response and stiffening of individual multiwalled carbon nanotubes. *Phys. Rev. Lett.* **89**, 255202 (2002).
16. Williams, P. A. *et al.* Fabrication of nanometer-scale mechanical devices incorporating multiwalled carbon nanotubes as torsional springs. *Appl. Phys. Lett.* **82**, 805–807 (2003).
17. Cumings, J. & Zettl, A. Low-friction nanoscale linear bearing realized from multi-walled carbon nanotubes. *Science* **289**, 602–604 (2000).
18. Yu, M.-F., Yakobson, B. I. & Ruoff, R. S. Controlled sliding and pullout of nested shells in individual multiwalled carbon nanotubes. *J. Phys. Chem. B* **104**, 8764–8767 (2000).
19. Cumings, J., Collins, P. G. & Zettl, A. Peeling and sharpening of multiwall nanotubes. *Nature* **406**, 586 (2000).
20. Collins, P. G., Arnold, M. S. & Avouris, P. Engineering carbon nanotubes and nanotube circuits using electrical breakdown. *Science* **292**, 706–709 (2001).
21. Poncharal, P., Wang, Z. L., Ugarte, D. & de Heer, W. A. Electrostatic deflections and electromechanical resonances of carbon nanotubes. *Science* **283**, 1513–1516 (1999).

Supplementary Information accompanies the paper on www.nature.com/nature.

Acknowledgements We thank N. Bodzin for assistance with graphics. This research was supported in part by the National Science Foundation, and by the Director, Office of Energy Research, Office of Basic Energy Sciences, Materials Sciences Division of the US Department of Energy.

Competing interests statement The authors declare that they have no competing financial interests.

Correspondence and requests for materials should be addressed to A.Z. (azettl@physics.berkeley.edu).